

Research Paper

## Identification of the planetary magnetosphere boundaries with the wavelet multi-resolution analysis

Mauricio José Alves Bolzan <sup>a,\*</sup>, Ezequiel Echer <sup>b</sup>, Adriane Marques de Souza Franco <sup>b</sup>, Rajkumar Hajra <sup>c</sup>

<sup>a</sup> Space Physics and Astronomy Laboratory (LAFEJ), Federal University of Jataí (UFJ), BR 364, Km 195, n. 3800, Jataí, Brazil

<sup>b</sup> National Institute for Space Research (INPE), São José dos Campos, Brazil

<sup>c</sup> Indian Institute of Technology Indore, Simrol, Indore 453552, India

ARTICLE INFO

Keywords:

Planetary magnetosphere  
Planetary bow shocks  
Planetary magnetopauses  
Haar wavelet  
Solar wind  
Wavelet analysis

ABSTRACT

The study of the properties and variations of planetary boundaries such as magnetosheaths and bow shocks is an important subject for magnetospheric dynamics and interaction with solar wind. The identification of these boundaries is important for those studies. Thus, the Haar wavelet decomposition technique is used to detect the planetary magnetosphere boundaries and discontinuities. We use the magnetometer data from the CASSINI and MESSENGER spacecraft to identify the abrupt changes in the magnetic field when the spacecraft crossed the magnetospheric bow shocks and magnetopauses of Saturn and Mercury, respectively. The methodology based on variance obtained by scale and edge identifications was shown to be a simple tool to perform this task. The results confirm that the Haar transform can efficiently identify the planetary magnetosphere boundaries characterized by the abrupt magnetic field changes. Due to this wavelet function to be a discrete function it promotes the abrupt and sharp identification of the boundaries. It is suggested that this technique can be applied to detect the planetary boundaries as well as the discontinuities such as the shock waves in the interplanetary space.

### 1. Introduction

Planetary magnetospheres are created as a result of interaction between the solar wind and the planetary magnetic field and plasma environment. Interaction of the solar solar wind with a magnetized planet creates an “intrinsic” magnetosphere. For a non-magnetic planet, the solar wind is deflected by the ionized atmosphere (ionosphere) and a magnetosphere is “induced” due to the generation of currents in its atmosphere/ionosphere by the magnetized solar wind plasma flow (Kivelson, 2007). As a planetary magnetosphere in the heliosphere is embedded in the supermagnetosonic plasma (solar wind) that continuously escapes from the Sun’s atmosphere, a stand bow shock (BS) is formed upstream of the planet. Following the BS, the solar wind is shocked, decelerated, heated and deflected in a region called magnetosheath. This region extends from the BS to the magnetopause (MP), the latter being the outer boundary of the planetary magnetosphere where the planetary magnetic field and plasma dominate (Stern and Ness, 1982; Russell, 2001). The magnetospheric shape, size and positions of the boundaries (BS and MP) depend on the solar wind and internal

(magnetosphere) conditions, and can be highly variable owing to the solar wind variations (Russell, 2001). The magnetospheric size (or the MP location) is mainly determined by the planetary magnetic field intensity and the solar wind density in the planet orbit (Kivelson and Bagenal, 2007). As the solar wind density at Mercury’s orbit is very high (Mercury being the nearest planet to the Sun, at ~0.4 astronomical unit (au) distance) and the magnetic dipole of the planet is weak (~0.003 Gauss at the equator), the magnetosphere of Mercury is very small and its magnetopause is generally found at about 2 R<sub>me</sub> (Mercury radii, ~2438 km) upstream the planet (Slavin, 2004). The solar wind Mach number ( $M_{ms}$ , the ratio of the solar wind speed  $V_{sw}$  to the local magnetosonic speed  $V_{ms}$ ) at Mercury is very low (~2–5, for comparison,  $M_{ms}$  near Earth varies between ~5 and 15), and consequently the properties of BS and magnetosheath are very susceptible to the variations in the upstream solar wind (Slavin et al., 2020).

The Saturn’s magnetosphere (at ~9.5 au from the Sun) is a complex system that has components from multiple physical sources (André et al., 2005). The magnetosphere is fast rotating and has a strong internal source of material from the moons deep within the planetary

\* Corresponding author.

E-mail address: [mauricio\\_bolzam@ufg.br](mailto:mauricio_bolzam@ufg.br) (M.J.A. Bolzan).

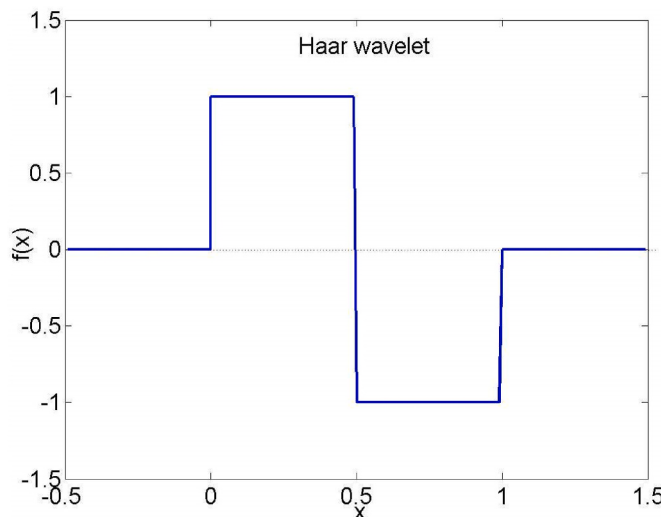


Fig. 1. The Haar wavelet function.

system. Furthermore, the planet is embedded in the solar wind, and there are momentum, energy and mass exchanges with the solar wind (Southwood and Chané, 2016). Internal plasma sources of the Kronian magnetosphere include the rings, icy satellites and Titan and Saturn's upper atmosphere and ionosphere. Recently, Jackman et al. (2019) analyzed 13 years of the CASSINI measurements in order to study Saturn's BS and MP boundaries. They indicated the difficulty to determine the BS and MP under a range of solar wind driving conditions. This is suggested to be significantly contributed by the moon Enceladus which acts as a significant internal source of plasma (Waite et al., 2006).

Besides investigations of the physical factors that can influence a planetary magnetosphere, there are several attempts to develop some tool to detect the planetary magnetospheric boundaries. For example, Martinecz et al. (2008), using data from Venus Express, proposed a 3-parameter fit in order to identify the shape of the Venus BS. They concluded that the BS position is relatively stable, while the night side ion composition boundary position is highly variable. Jelínek et al. (2012), using data from the THEMIS spacecraft, developed a method useful to be used for development of the magnetopause and BS models, but without necessity to identify the boundary crossings. This is an indicative of the difficult to identify these boundary crossings. Jelínek et al. (2012) have developed an automated method for identifications of bow shock and magnetopause positions, which was validated through visual inspection of THEMIS data. This method is based on the ratios of spacecraft measurements in these regions and upstream solar wind observations. In this work, we present a wavelet technique to identify the abrupt changes in the magnetic field at the magnetospheric boundary crossings. This technique decomposes the magnetic field data in frequency levels using the multi-resolution analysis (MRA). For this purpose, we analyzed the magnetic field measurements made by CASSINI during its Saturn orbit insertion in 2004, and by MESSENGER during its first Mercury flyby in 2008. Both Saturn and Mercury are planets with intrinsic magnetospheres. The main aim of this work is to develop and demonstrate a technique to efficiently identify the planetary (magnetospheric) boundaries and discontinuities in the space plasma, which can be used as an important tool in space research.

## 2. Database and method of analysis

In order to identify the BS and MP boundaries of Mercury and Saturn,

we used two conjugate approaches, namely, the wavelet analysis to decompose the magnetic field vector component time series in dyadic scales, and the variance by scale analysis to identify the scales with the maximum energy obtained through of the spectral power. The variance by scale is an important approach to identify the sharp/abrupt changes in the magnetic field, and can be used to remove the long-term periodicities of the time series (see Bolzan et al., 2020). Bolzan et al. (2020) used the Daubechies wavelet as this is more efficient in removing scales compared to, for example, the Haar wavelet (Bolzan et al., 2009). However, the Haar wavelet is able to better identify the sharp changes in the time series compared to the Daubechies function. Thus, Haar wavelet decomposition technique will be used in the present work.

### 2.1. Wavelet analysis

Similar to the Fourier analysis, which decomposes a signal in sine wave components of different frequencies, the wavelet transform decomposes a time series in translated and scaled (dilated or compressed) versions of the mother wavelet, each one multiplied by an appropriate coefficient (Kumar and Foufoula-Georgiou, 1997; Torrence and Compo, 1998).

Recently, wavelet analysis has been widely employed to study the non-stationary process in the time series analysis, such as the interplanetary shocks (Gedalin et al., 1998) and waves/turbulence in the planetary magnetospheres (Tarasov et al., 1998; Espley et al., 2004; Bolzan et al., 2005; Echer, 2009, 2010; Franco et al., 2020). Of special interest are the orthonormals, discrete wavelet transforms, which are used in multi-resolution analysis (MRA) (Kumar and Foufoula-Georgiou, 1997; Echer, 2004).

The wavelet transform is a very powerful tool to analyze the non-stationary signals, and it is used to obtain expansions of a signal using the time-localized functions (wavelets) that have good properties of localization in time and in frequency domain (Kumar and Foufoula-Georgiou, 1997; Percival and Walden, 2000). The wavelet transform may be continuous or discrete. While the continuous wavelet transform calculates coefficients at every possible scale, the discrete wavelet transform chooses scales and positions based on the power of the dyadic scales and positions. Thus, the discrete wavelet is a subsampling of the continuous one at just the dyadic scales  $2j - 1$ ,  $j = 1, 2, \dots$ , etc. Therefore, the discrete wavelet transform may be used in MRA, which is concerned with the study of signals or processes represented at different resolutions, and the development of an efficient mechanism for going from one resolution to another (Percival and Walden, 2000).

In MRA (or multiple level decomposition), a signal ( $S$ ) is broken down interactively into many lower resolution components. This decomposition process, with successive approximations being decomposed in turn, is called the wavelet decomposition tree.  $S$  is split into an approximation  $A$  and a detail  $D$ .  $D$  contains the high-frequency part of the signal, whereas  $A$  contains most of the characteristic frequencies in  $S$ . In the first step of the decomposition,  $S = A_1 + D_1$ . In the next step, the approximation itself is split into a second level approximation:  $A_1 = A_2 + D_2$ , and so on. The process is equivalent to a filtering procedure: in the first step, the signal has a low-pass filtered component ( $A_1$ ), and a high-pass filtered component ( $D_1$ ).  $A_1$  is then itself split, and one has the  $D_2$  level as a band-pass filtered data. The numbers of the allowed levels depend on the length of the signal that corresponds to the dyadic order as mentioned. Thus, if a signal has 8 numbers, it is possible to decompose it in three levels in order to obey the dyadic relation given by  $2^3 = 8$  numbers.

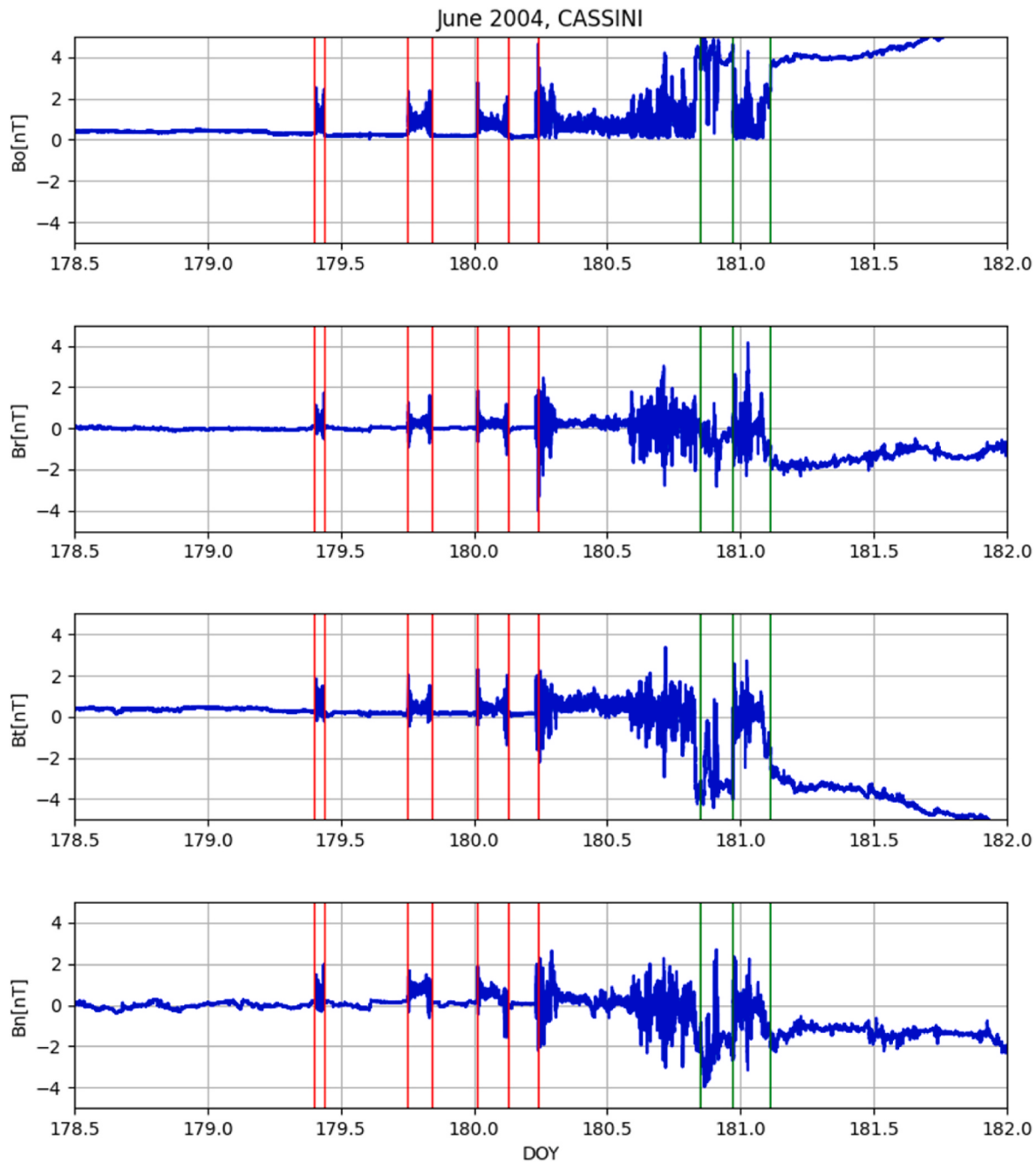


**Fig. 2.** Near-Saturn magnetic field measurements by the CASSINI spacecraft during its inbound trajectory between 27 and 29 June 2004. The BS and MP crossings are indicated by the red and green vertical lines, respectively.

## 2.2. Haar wavelet

In this work, the Haar wavelet is used to decompose the magnetic field vector data. Fig. 1 shows a plot of this wavelet function. Since it is a discontinuous function, it should be an adequate basis to study the abrupt, discontinuous variations such as the planetary BS and MP crossings. The Haar wavelet is one of the most used orthogonal wavelet families that are used for filtering/decomposition of the time series. The Haar function is orthogonal, with dilation being dyadic in the form:  $a =$

$2^{-j}$ , and its translations occur in discrete steps, in the form:  $b = 2^{-j} k$ , where  $j$  and  $k$  are integers. This wavelet function is given by:

$$\psi_{j,k}(t) = \begin{cases} 2^{j/2}, & \dots, 2^{-j}k < t < 2^{-j}k + 1/2 \\ -2^{j/2}, & \dots, 2^{-j}k < t < 2^{-j}k + 1 \\ 0, & \dots, \text{all other values of } t \end{cases} \quad (1)$$

The Haar wavelet function is inserted inside the Wavelet Transform (WT) in order to decompose any non-stationary time series in dyadic scales according to equation:

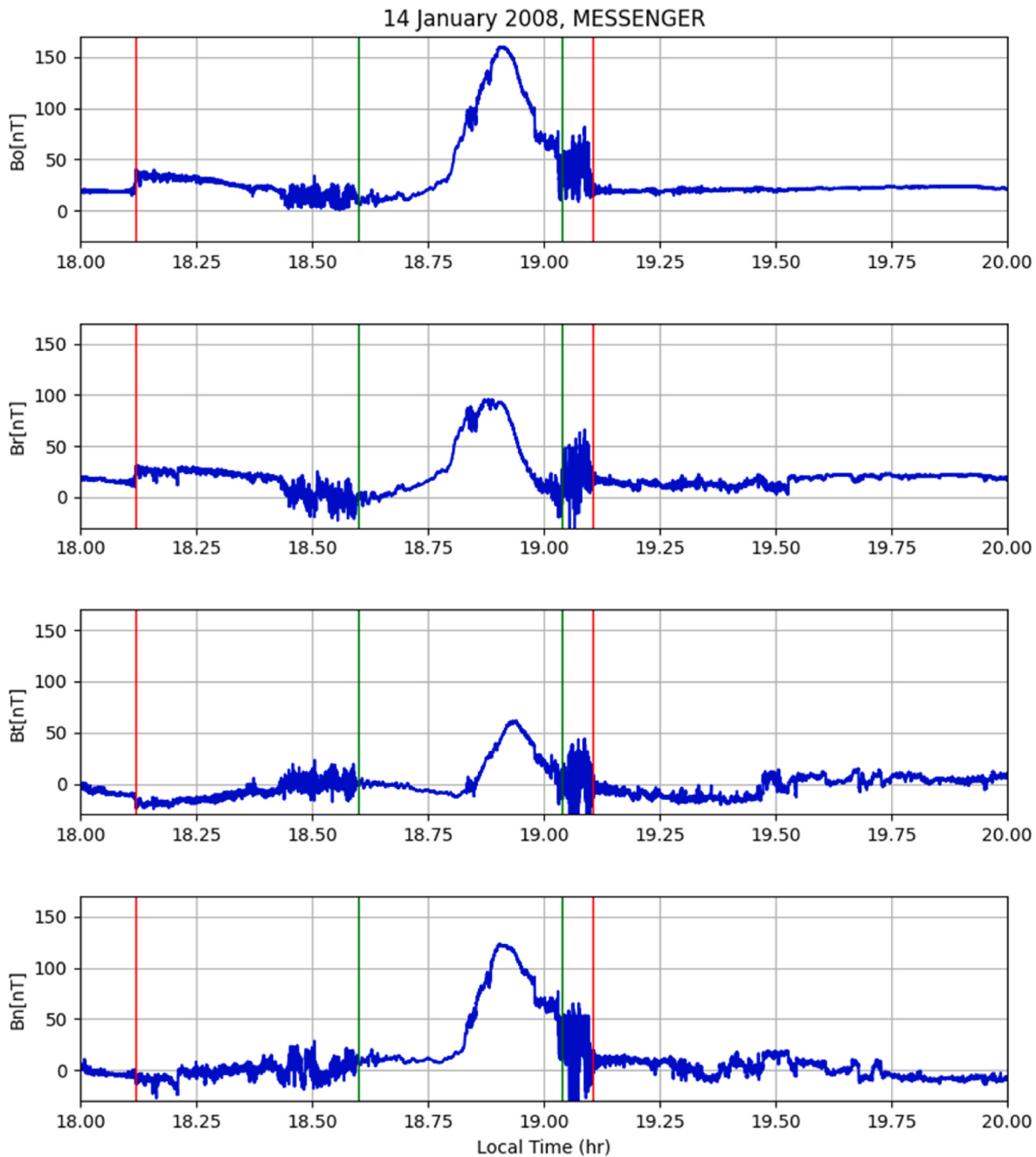


**Fig. 3.** Near-Mercury magnetic field measurements by the MESSENGER spacecraft during its first Mercury flyby on 14 January 2008. The BS and MP crossings are indicated by the red and green vertical lines, respectively.

$$WT = \int f(t)\Psi_{j,k}(t)dt \quad (2)$$

where  $f(t)$  is the time series and  $\Psi_{j,k}(t)$  is the Haar wavelet function.

### 2.3. Magnetometer data

The high-resolution (5 s) CASSINI fluxgate magnetometer data (Dougherty et al., 2004), and the MESSENGER magnetometer data

(Anderson et al., 2007) explored in this work were obtained from NASA's Planetary Data System (PDS, <http://pds.jpl.nasa.gov/>). This 5s resolution was selected because it is high enough to investigate the BS and MP crossings. The interplanetary magnetic field (IMF) measurements are performed in the radial tangential normal (RTN) coordinate system, where  $\hat{R}$  directed from the Sun to the spacecraft,  $\hat{T} = \Omega X \hat{R} / |\Omega X \hat{R}|$ , where  $\Omega$  is the solar rotation axis.

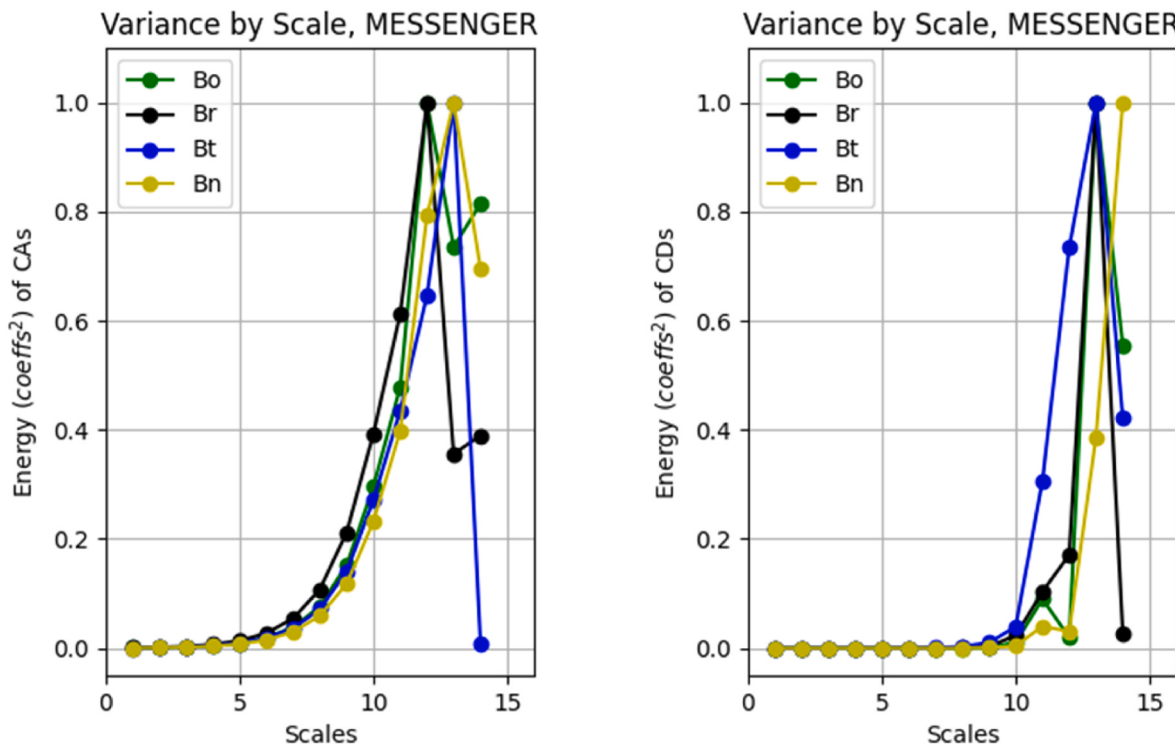


**Fig. 4.** Variance by scale for the magnetic field measurements by MESSENGER during its Mercury flyby shown in Fig. 3. Left and right panels show the variances of CAs and CDs, respectively.

### 3. Results and discussions

#### 3.1. Original data

The CASSINI spacecraft reached the near-Saturn environment during the end of June 2004 and made its first crossing of the planetary orbit (Dougherty et al., 2004, 2005). Saturn's magnetosphere is characterized by large variations in its BS and MP boundaries due to the internal factors and the solar wind pressure (Jackman et al., 2019). According to Dougherty et al. (2005), a total of 17 bow shock and 7 magnetopause crossings on the inbound and outbound passages were measured. But it is important to note that the bow shock crossings were identified by abrupt increases in the magnetic field magnitude where the solar wind was compressed and decelerated. So, identification of these physical boundaries in the automatic way is important to study and understand the internal factors like the planetary periodic oscillations.

Fig. 2 shows the magnetic field components (trend removed) measured by the CASSINI magnetometer during its inbound trajectory between 27 and 29 June 2004. The BS and MP crossings are indicated by the red and green lines, respectively. The Saturn magnetosphere size was observed to be highly variable during this period, with 7 BS and 3 MP crossings (Dougherty et al., 2005; Achilleos, 2006). The BS crossings can be identified by the abrupt jumps in the magnetic field magnitude  $B_o$ . The region downstream of the BS exhibits large fluctuations in magnetic field components, indicating the magnetosheath. The MP crossings are identified by an enhancement in  $B_o$  and by abrupt directional changes in the magnetic field components. Most of the BSs crossed during this period were found to be of the quasi-perpendicular type (Achilleos, 2006). The BS and MP subsolar distances were found to be at ~40–49 Saturn radii (Rs) and ~30–34 (Rs), respectively (Dougherty et al., 2005).

The MESSENGER spacecraft made the first of its three flybys of Mercury on 14 January 2008 (Echer, 2010; Slavin et al., 2008), and measured the near-Mercury magnetic field (Anderson et al., 2007). This is shown in Fig. 3 where we removed the trend from the time series. MESSENGER, in its inbound trajectory, detected a BS, which was crossed at 18:08:38 UT (inbound) and 19:18:55 UT (outbound) on 14 January. Before the inbound MP crossing at 18:43:02, the last extended interval of the southward magnetic field ended at 18:38:40. After MESSENGER exit of the magnetosphere, the magnetic field was observed to be generally northward.

#### 3.2. Decomposed data

The MESSENGER magnetic field magnitude  $B_o$  and vector components  $B_r$ ,  $B_b$ ,  $B_n$  data during the ~1 h Mercury flyby were decomposed in orthonormal frequency levels using the Haar wavelet transform. The magnetic field data were decomposed in 14 scales according to data length used.

We performed the variance by scale in order to identify the scale with the maximum energy. In order to determine this scale we have employed the global wavelet spectrum (GWS) to the magnetic field vector data. Fig. 4 shows the variance by scale for the wavelet coefficients A and D (CAs and CDs) of  $B_o$  and components  $B_r$ ,  $B_b$ ,  $B_n$ . It can be clearly seen that most of the energy for the wavelet coefficients (CAs and CDs) is concentrated at large scales, between the scales 11 and 14.

As the maximum energy is found to be concentrated between the scales 11 and 14, CAs and CDs for the scales from 1 to 10 are assigned the value 0. This implies that the scales 1–10 do not contribute significantly to the total energy. However, the coefficients CAs and CDs were maintained from scale 11 onward. The magnetic field time series is

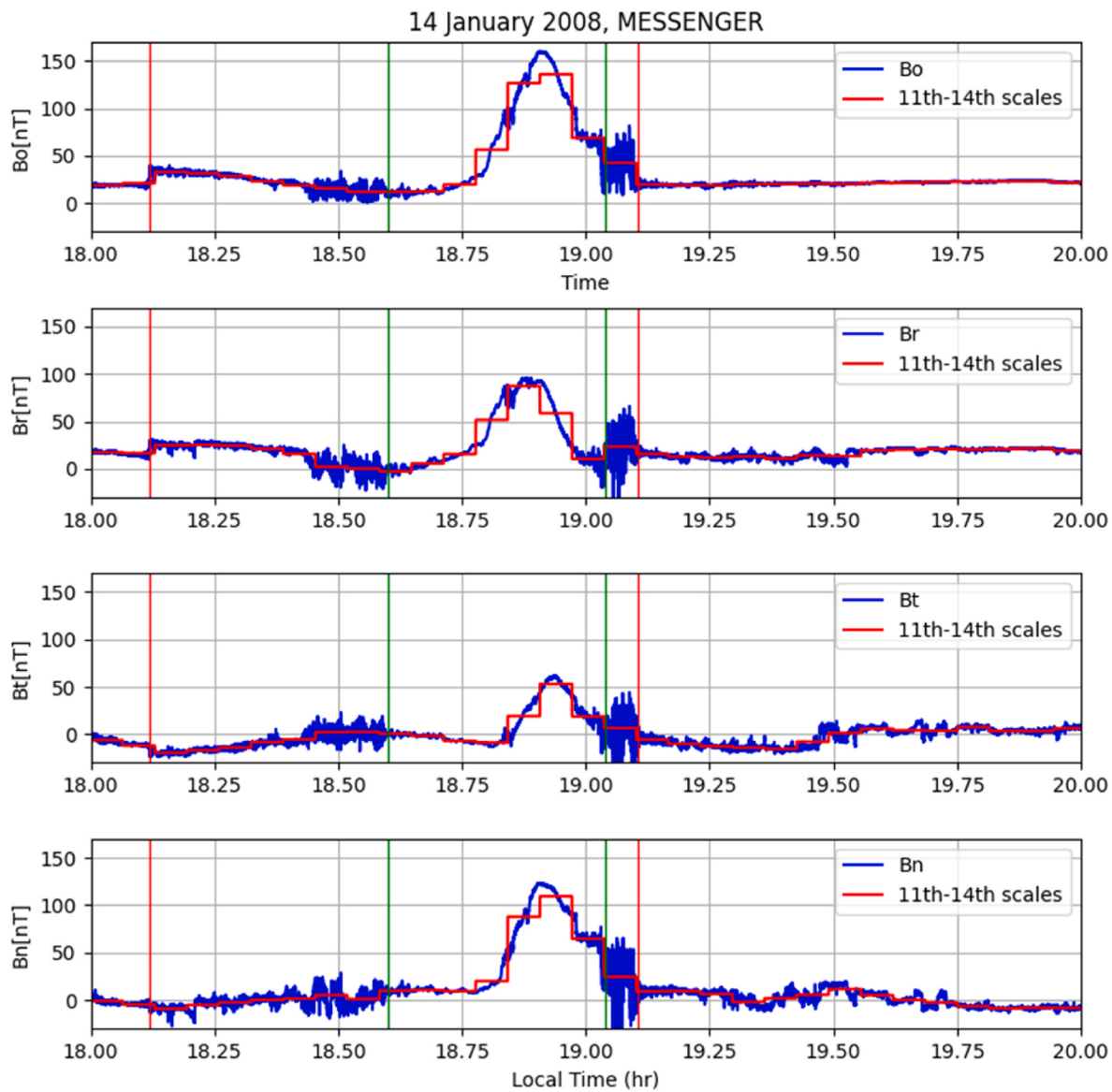


**Fig. 5.** Comparison between the reconstructed magnetic field (red) with the MESSENGER measurements (blue) shown in Fig. 3. The BS and MP crossings are indicated by the red and green vertical lines, respectively.

reconstructed accordingly using the CAs and CDs for scales 11–14. Fig. 5 shows the reconstructed magnetic field (in red) along with the original measurements (blue) for the Messenger magnetometer measurements in Mercury. The sharp changes in the magnetic field corresponding to the BS and MP crossings can be clearly identified in the reconstructed data using the coefficients CAs and CDs from scales 11 to 14.

We applied the same procedure, as above, to the CASSINI magnetic field data (for Saturn encounter). The CASSINI data were decomposed in 15 scales. Fig. 6 shows the variance by scale of the CAs and CDs coefficients (of the three magnetic field components and magnitude). The magnetic field variances increase from scale 11 and attain the maximum value at scale 15 for both wavelet coefficients. This implies that most of the energy is concentrated at large scales, from 11 to 15.

Again, we used the same methodology (as applied to the MESSENGER data), by assigning zero to the CAs and CDs for scales 1–10, and those for scales 11–15 are maintained. The magnetic field time

series is reconstructed accordingly using the CAs and CDs of scales 11–15. Fig. 7 compares the original and reconstructed magnetic fields. Clearly, the reconstruction of the magnetic field using only scales 11 to 15 is able to identify the majority of the sharp changes associated with BS and MP crossings.

Figs. 8 and 9 show the MRA decomposition levels only for the magnetic field magnitude  $B_o$  from CASSINI and MESSENGER, respectively. The same decomposition levels were computed for magnetic field components but are not shown for sake of brevity and to avoid repetition. The top panels correspond to the original data, followed by different decomposition levels in the lower panels and the reconstructed data in the bottom panels. A comparison between the top and bottom panels confirms the identical shape (variation) of the original and reconstructed data. It is important to mention that the low frequency variations are the envelope of the variations, since high frequencies are filtered in the decomposition levels. Thus, we have only these low

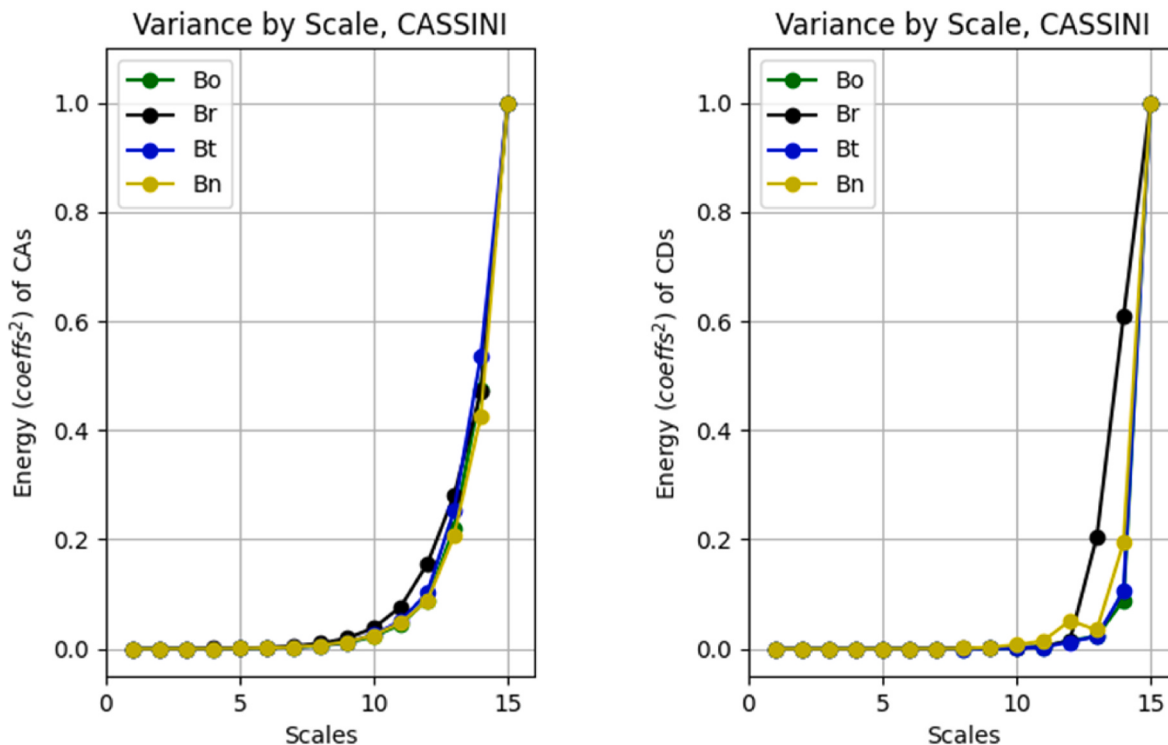


**Fig. 6.** Variance by scale for the magnetic field measurements by CASSINI during its first Saturn flyby shown in Fig. 2. Left and right panels show the variances of CAs and CDs, respectively.

frequency variations which are used to identify the BS and MP crossings.

### 3.3. Finding the edges

As it is possible to observe in Figs. 5 and 7 the time series reconstructed show an evident sharp variation between the MS and BS boundaries, for both spacecraft data. Thus, the next step was to find these edges. The methodology consists to calculate the differences between two consecutive data points such as  $\Delta s(t) = s(t+1) - s(t)$ . Fig. 10 shows the results for CASSINI's data, where we can note that the edges indicate the exact location of the boundary limits. It is important to note also there are differences in the magnitudes of the edges between BS and MP. This fact is important because it can help us to create a threshold using these edge differences in order to identify and separate both BS and MP crossings. Thus, due to the different magnitudes between edges from BS and MP, we separated the time series in two parts in order to apply a threshold to find out only the edges responsible for each boundary limits.

Figs. 11 and 12 show the edges before and after filtering processes to CASSINI data. An important result found is due to the fact that the edges that remains after the filtering process have a good agreement with the BS and MP boundaries. However, it is possible to note that these results depend on the magnetic field component and the value used for the threshold, i.e., we did not find the same behavior for all components analyzed and for the two boundaries. This point is also important and it indicates that is necessary to find out a way to obtain the same results for all components (or other variables). Anyway, the methodology employed here has shown that it is possible to use a computational approach, based on wavelet analysis, in order to find the boundaries of MP and BS.

It is important to note also the threshold used should depend on the magnetic field component used and of the kind of boundary (BS or MP) as shown in Fig. 10. However, different values would increase the complexity of this present method proposed. Thus, in order to simplify the analysis we adopted the same values of the threshold for components from BS and another values for components from MP, i.e., we used different threshold values between BS and MP.

### 4. Summary and Conclusions

In this work we presented a wavelet technique to identify the abrupt changes in the magnetic field at the magnetospheric boundary crossings (bow shock and magnetopause). The Haar wavelet was used to decompose the magnetic field data in different frequency levels. We analyzed the magnetic field measurements by CASSINI spacecraft during its Saturn orbit insertion, and by MESSENGER during its first Mercury flyby in 2008. The Haar wavelet multiresolution analysis (MRA) was employed in this work to decompose the CASSINI and MESSENGER magnetometer data in orthonormal frequency levels. The objective was to identify the abrupt changes in the magnetic field when CASSINI and MESSENGER crossed the magnetospheric BS and MP of Saturn and Mercury, respectively. We have found that the Haar transform can be used to identify this type of abrupt boundaries.

In summary, the results obtained with the methodology proposed in this work are the following:

1. We applied the WT in order to decompose the time series by scales;
2. We calculated the variance by scales in order to find out the scales where the energy is maximum;

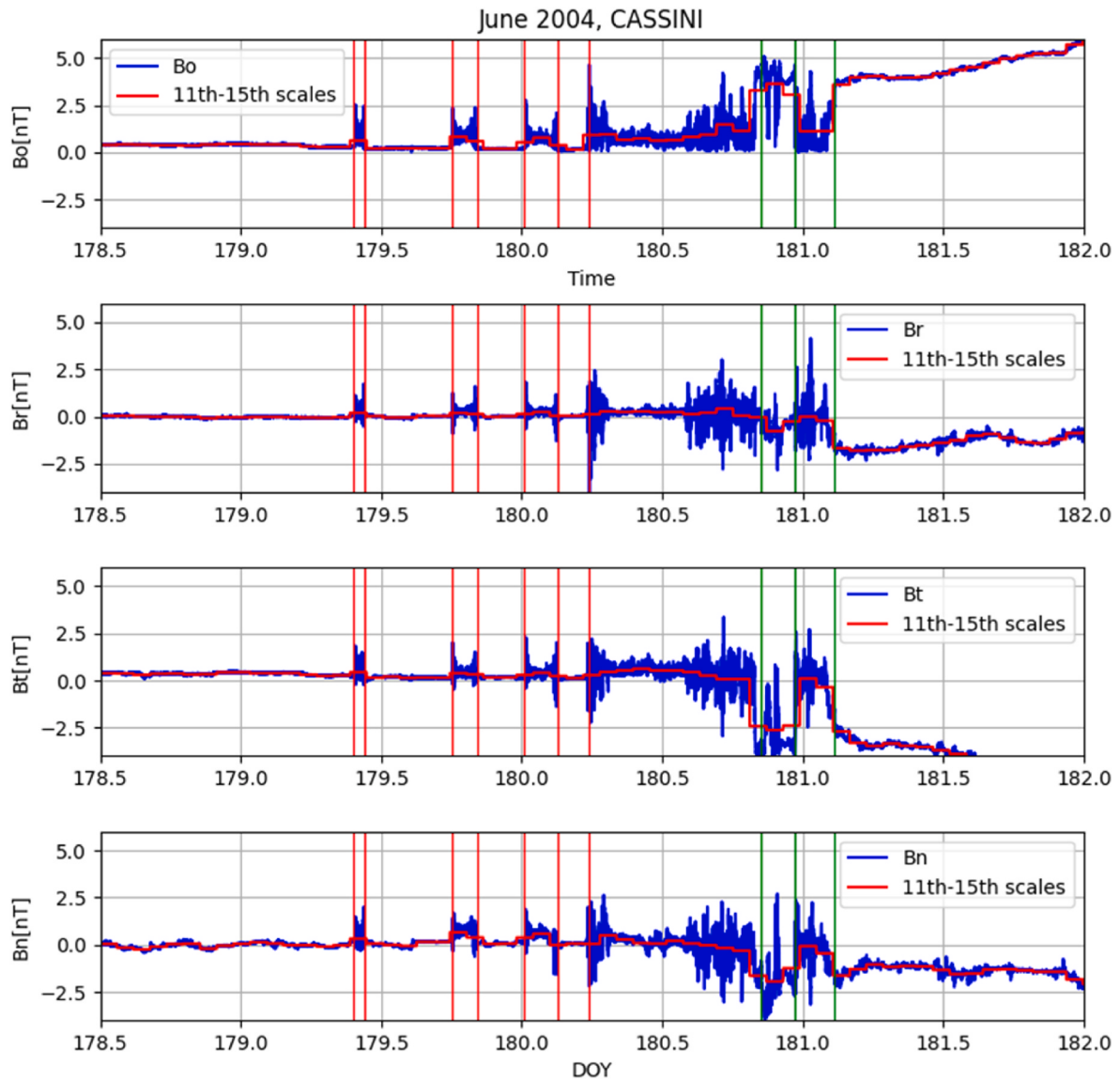


**Fig. 7.** Comparison between the reconstructed magnetic field (red) with the CASSINI measurements (blue) shown in Fig. 2. The BS and MP crossings are indicated by the red and green vertical lines, respectively.

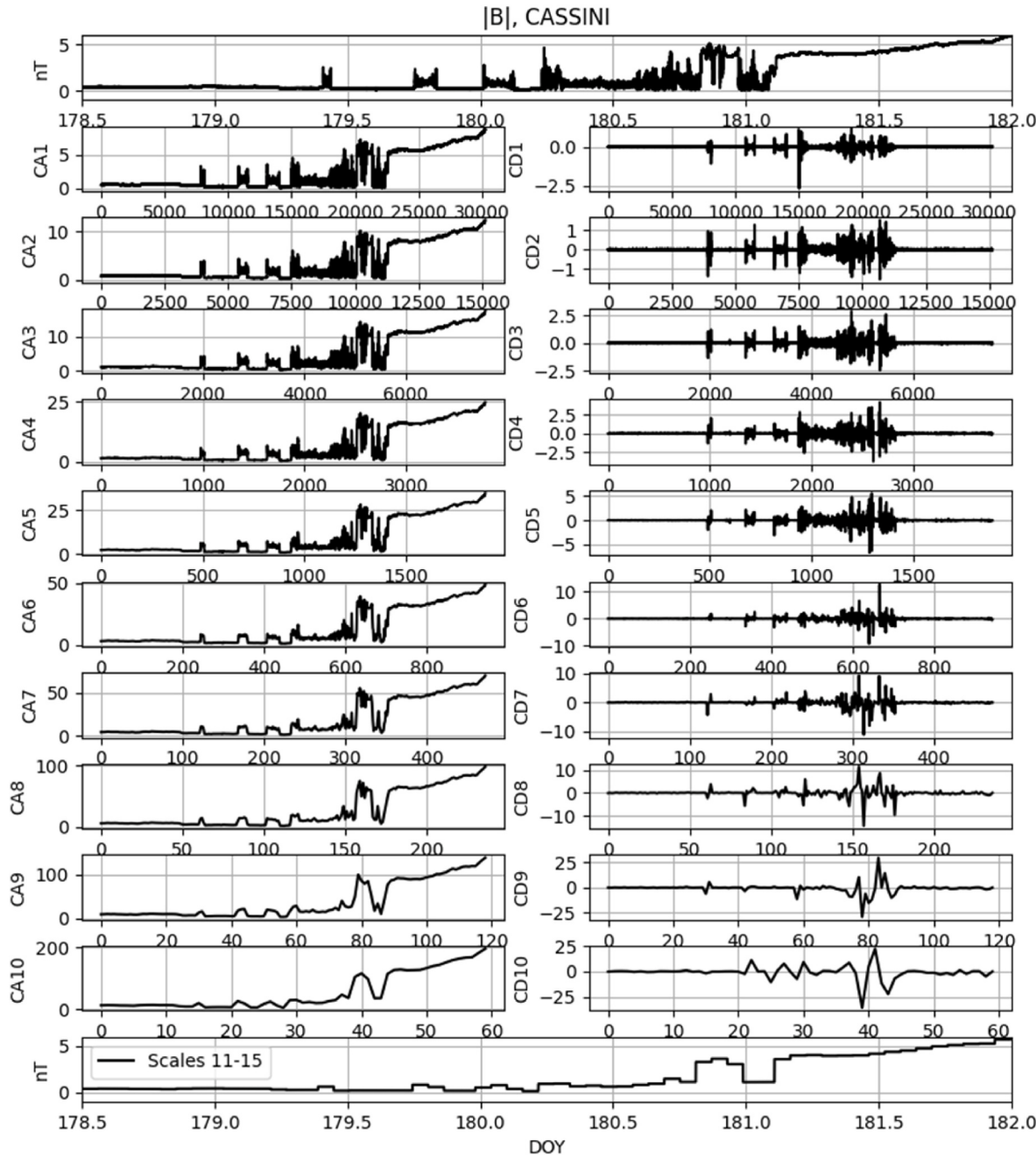


**Fig. 8.** The Haar wavelet decomposition levels for the CASSINI magnetic field magnitude. Top panel shows the original measurement, followed by the MRA decomposition coefficients CA1 to CA10 (left panels), and CD1 to CD10 (right panels), and the reconstructed data in the bottom panel.

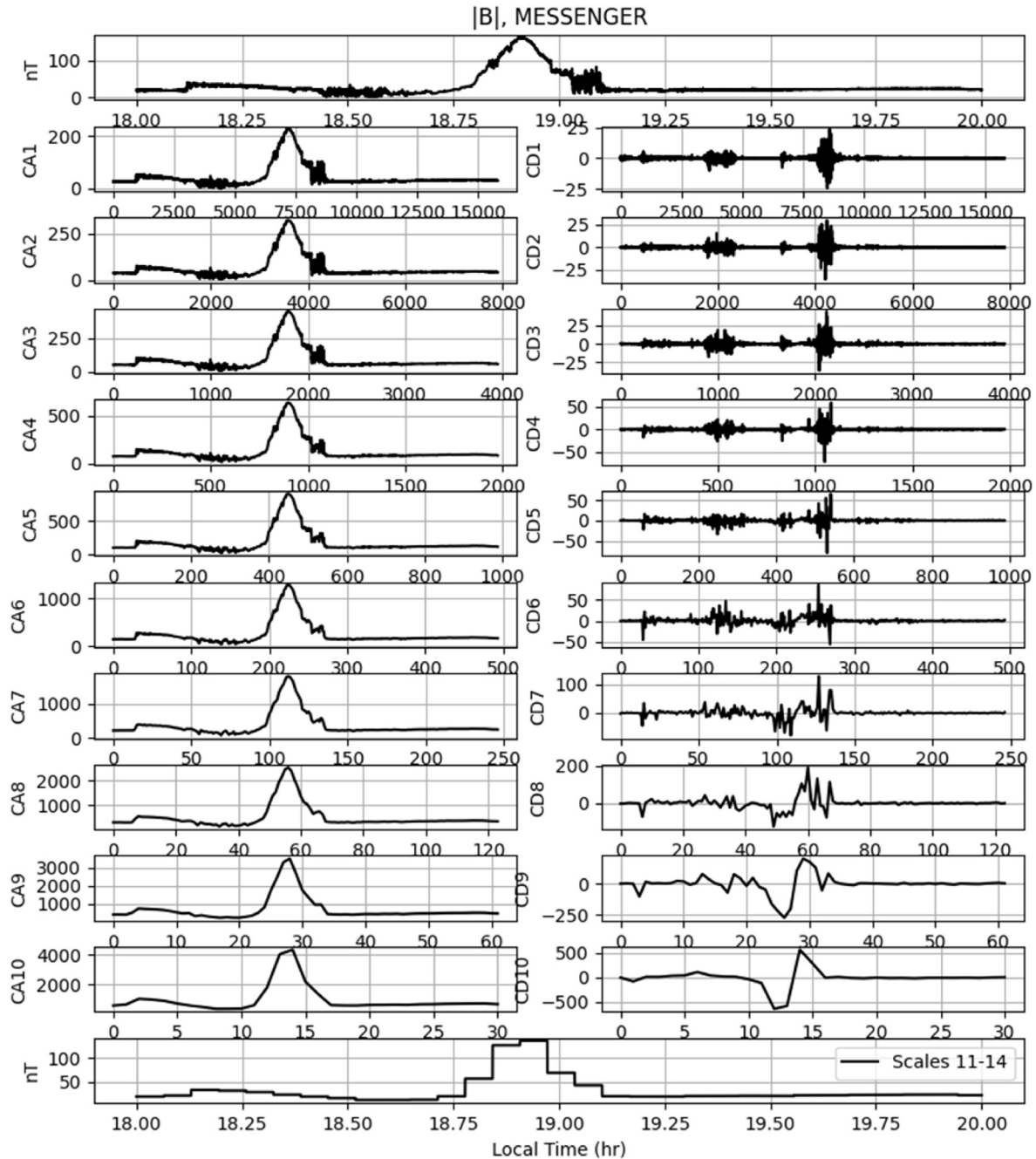


**Fig. 9.** The Haar wavelet decomposition levels for the MESSENGER magnetic field magnitude. The panels are in the same format as in Fig. 8.

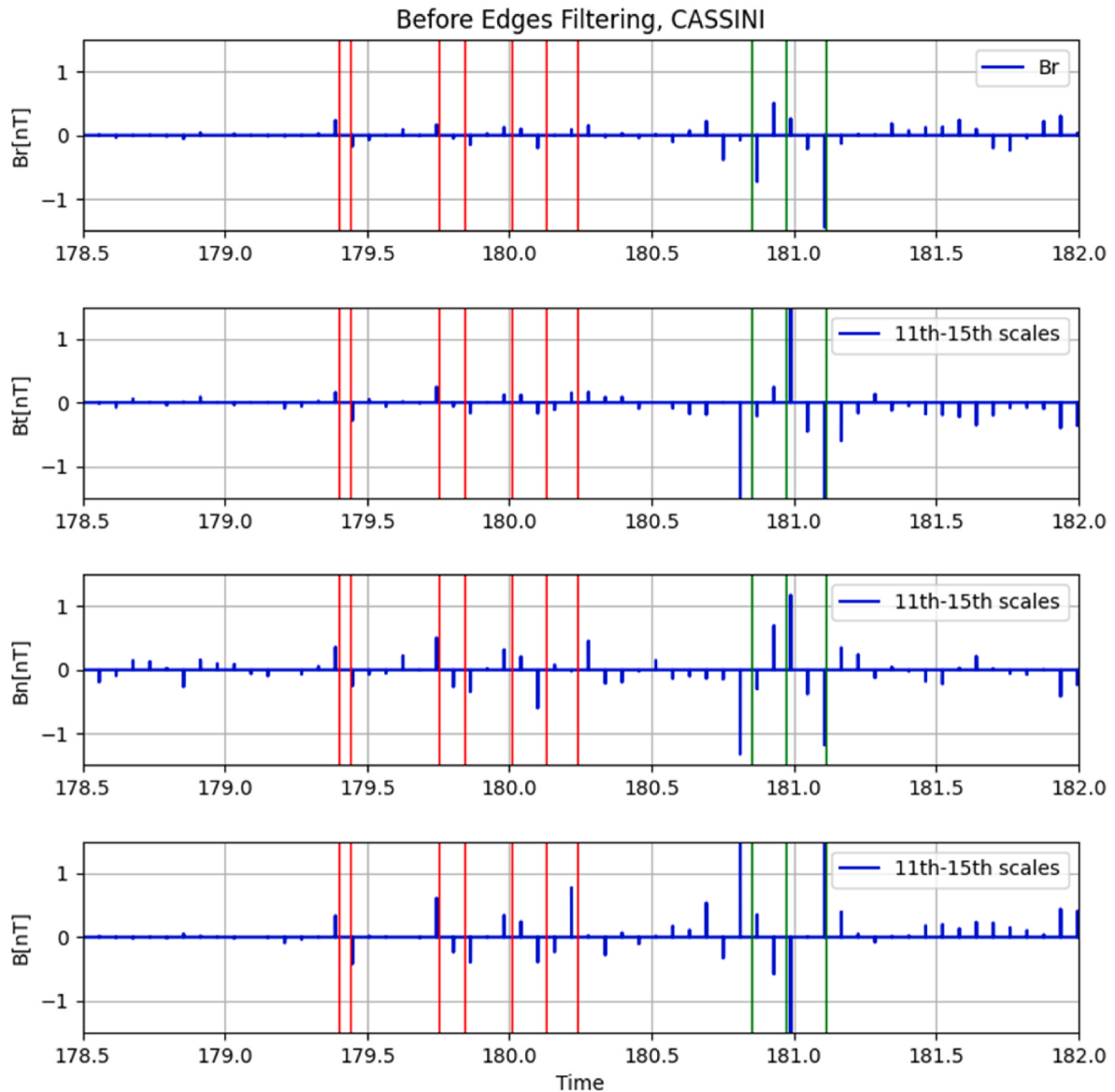
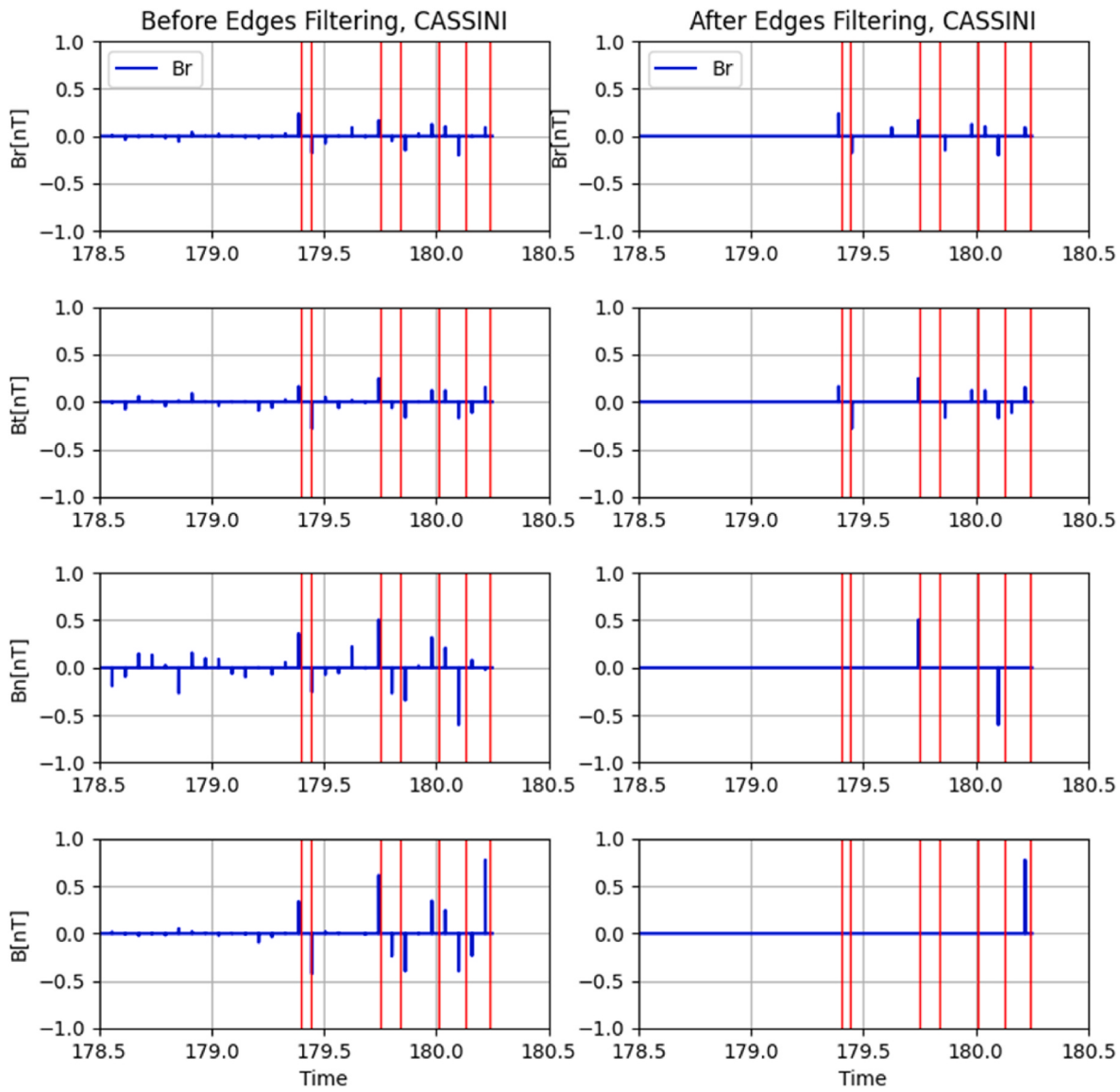


Fig. 10. The edges found to CASSINI data. It is possible to note the magnitude of the edges from BS and MP are different.



**Fig. 11.** The edges before and after filtering processes to CASSINI data. The vertical red line indicates the BS.

3. After that, the CAs and CDs from scales 1 to maximum scale found in step 1 are assigned the value 0 for both spacecraft data. We performed this procedure because this implies these scales do not contribute significantly to the total energy;
4. We reconstructed the time series using the inverse wavelet transform;
5. To find the edges we calculated the difference between two consecutive data points given by  $\Delta s(t) = s(t+1) - s(t)$ ;
6. Finally, we applied a threshold in order to remove the small amplitude edges found in step 3.

From the results from the variance analysis by scale, it was possible to note that the maximum energy was found at different scales for each spacecraft, 10 up to 11 scales (1–3 h) for MESSENGER and the 15 scale

( $\geq 10$  h) for CASSINI. Thus, although CASSINI and MESSENGER have shown maximum energy obtained through of the spectral power results has shown this maximum energy values from each one were obtained in distinct scales. In fact, we used GWS because the maximum energy is obtained performing the variance by scale, in different scales, but as the BS MPB are abrupt or quasi abrupt changes, the timescales to detect them are similar.

The BS crossings have been identified from time-scales of  $\sim 10\text{--}20$  s to  $\sim 10\text{--}40$  min. However, time-scales of  $\sim 10\text{--}40$  min are more adequate to identify the BS crossings because much of the magnetic oscillations due to the magnetosheath waves are removed in these levels. On the other hand, multiple MP crossings are seen clearly only at  $\sim 3\text{--}10$  h time-scales. Further work should be conducted to use this technique to obtain quantitative information about the magnetospheric boundaries. This

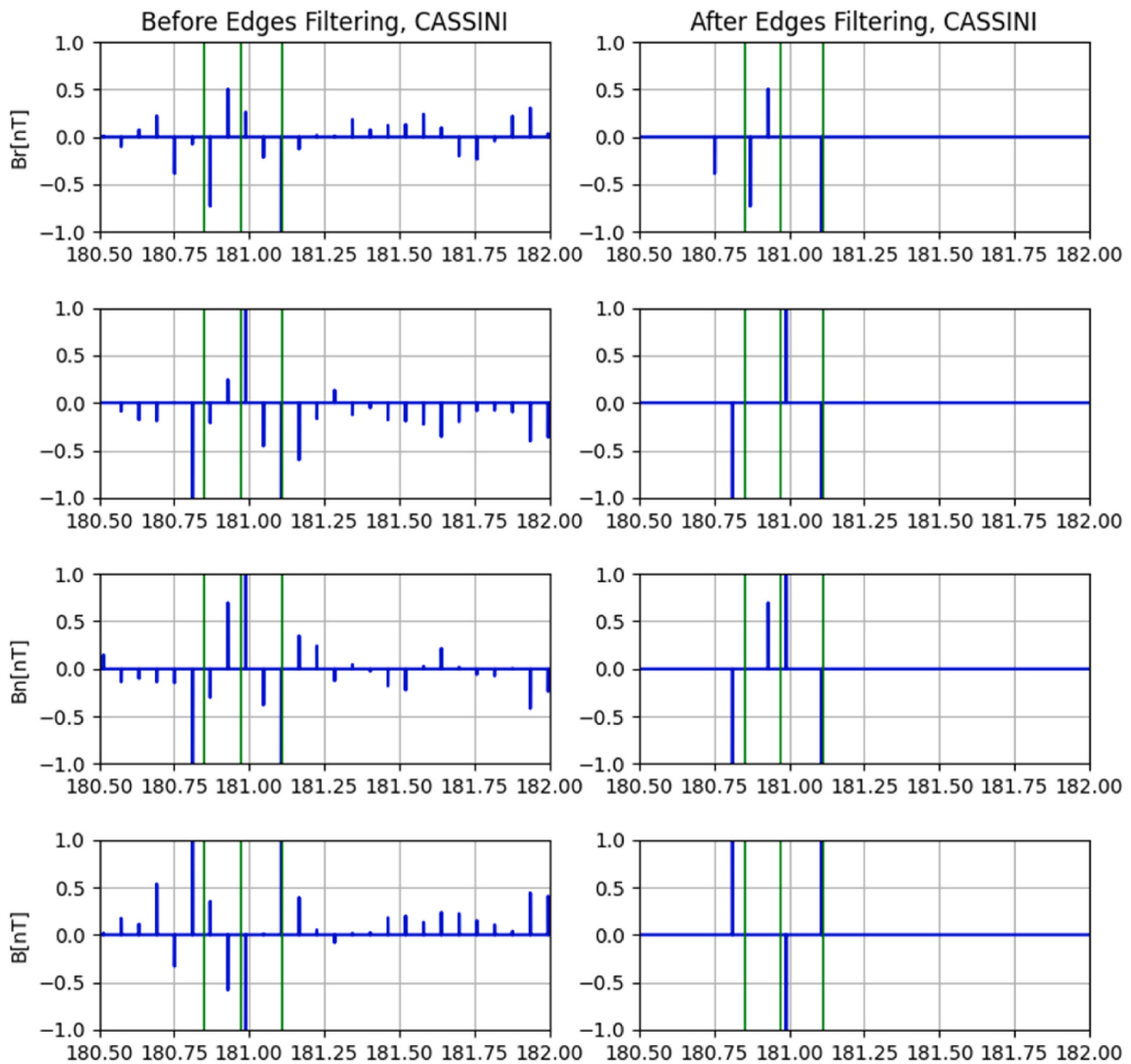


**Fig. 12.** The edges before and after filtering processes to CASSINI data. The vertical green line indicates the MP.

technique can be applied both to planetary boundaries as well as to detect discontinuities in the interplanetary space such as interplanetary shocks.

#### Author contributions

Conceptualization, M.J.A.B.; methodology, M.J.A.B.; validation, M.J.A.B.; formal analysis, M.J.A.B.; writing—original draft preparation, M.J.A.B.; writing—review and editing, E.E., A.M.S.F. and R.H.. All authors have read and agreed to the published version of the manuscript.

#### Data availability

The CASSINI and MESSENGER magnetometer data are obtained from NASA's Planetary Data System (PDS, <http://pds.jpl.nasa.gov/>).

#### Declaration of competing interest

The authors declare that they have no known competing financial interests or personal relationships that could have appeared to influence the work reported in this paper.

#### Acknowledgments

MJAB was supported by CNPq agency contract number (PQ-302330/2015-1 and PQ-305692/2018-6) and FAPEG agency contract number 2012.1026.7000905. AMSF thanks to CNPq agency (project 301969/2021-3) for the support. EE would like to thank Brazilian agencies for research grants: CNPq/PQ (302583/2015-7, 301883/2019-0) and FAPESP (2018/21657-1). The work of RH is funded by the Science and Engineering Research Board (SERB) (grant no. SB/S2/RJN-080/2018), a statutory body of the Department of Science and Technology (DST), Government of India through Ramanujan Fellowship.

## Abbreviations used

The following abbreviations are used in this manuscript

A	Approximation
BS	Bow shock
CA	Coefficient A
CD	Coefficient D
D	Detail
IMF	Interplanetary magnetic field
MP	Magnetopause
MRA	Multi-resolution analysis
PDS	NASA's Planetary Data System
R me	Mercury raii
R s	Saturn radii
RTN	Radial tangential normal coordinate system
S	Signal
UT	Universal time

## References

- Achilleos, N.e.a., 2006. Orientation, location and velocity of saturn's bow shock: initial results from the cassini spacecraft. *J. Geophys. Res.* 111 <https://doi.org/10.1029/2005JA011297> xx-xx.
- Anderson, B.J., Acuna, M.H., Lohr, D.A., Scheifele, J., Raval, A., Korth, H., Slavin, J.A., 2007. The magnetometer instrument on messenger. *Space Sci. Rev.* 131, 417–450. <https://doi.org/10.1007/s11214-007-9246-7>.
- André, N., Dougherty, M.K., Russell, C.T., Leisner, J.S., Khurana, K.K., 2005. Dynamics of the saturnian inner magnetosphere: first inferences from the cassini magnetometers about small-scale plasma transport in the magnetosphere. URL: *Geophys. Res. Lett.* 32 <https://doi.org/10.1029/2005GL022643>. arXiv:<https://agupubs.onlinelibrary.wiley.com/doi/pdf/10.1029/2005GL022643>. <https://agupubs.onlinelibrary.wiley.com/doi/abs/10.1029/2005GL022643>.
- Bolzan, M.J.A., Franco, A.M.S., Echer, E., 2020. A wavelet based method to remove the long term periodicities of geophysical time series. *Adv. Space Res.* 66, 299–306. <https://doi.org/10.1016/j.asr.2020.04.014>.
- Bolzan, M.J.A., Guarneri, F.L., Vieira, P.C., 2009. Comparisons between two wavelet functions in extracting coherent structures from solar wind time series. *Braz. J. Phys.* 39, 12–17. <https://doi.org/10.1590/S0103-97332009000100002>.
- Bolzan, M.J.A., Sahai, Y., Fagundes, P.R., Rosa, R.R., Ramos, F.M., Abalde, J.R., 2005. Intermittency analysis of geomagnetic storm time-series observed in Brazil. *J. Atmos. Sol. Terr. Phys.* 67, 1365–1372. <https://doi.org/10.1016/j.jastp.2005.06.008>.
- Dougherty, M.K., Achilleos, N., Andre, N., Arridge, C.S., Balogh, A., Bertucci, C., Burton, M.E., Cowley, S.W.H., Erdos, G., Giampieri, G., Glassmeier, K.H., Khurana, K.K., Leisner, J., Neubauer, F.M., Russell, C.T., Smith, E.J., Southwood, D.J., Tsurutani, B.T., 2005. Cassini magnetometer observations during saturn orbit insertion. *Science* 307, 1266–1270. <https://doi.org/10.1126/science.1106098>.
- Dougherty, M.K., Kellock, S., Southwood, D.J., Balogh, A., Smith, E.J., Tsurutani, B.T., Gerlach, B., Glassmeier, K.H., Gleim, F., Russell, C.T., Erdos, G., Neubauer, F.M., Cowley, S.W.H., 2004. The cassini magnetic field investigation. *Space Sci. Rev.* 114, 331–338. <https://doi.org/10.1007/s11214-004-1432-2>.
- Echer, E., 2004. Multi-resolution analysis of global total ozone column during 1979–1992 nimbus-7 toms period. *Ann. Geophys.* 22, 1487–1493. <https://doi.org/10.5194/angeo-22-1487-2004>.
- Echer, E., 2009. Foreshock and magnetosheath waves at uranus and neptune studied with wavelet analysis. *Adv. Space Res.* 44, 1030–1037. <https://doi.org/10.1016/j.asr.2009.05.024>.
- Echer, E., 2010. Wavelet analysis of ulf waves in the mercury's magnetosphere. *Rev. Bras. Geofis.* 28, 175–182. <https://doi.org/10.1590/S0102-261X2010000200003>.
- Espley, J.R., Cloutier, P.A., Brain, D.A., Crider, D.H., Acuna, M.H., 2004. Observations of low-frequency magnetic oscillations in the marginia magnetosheath, magnetic pileup region and tail. *J. Geophys. Res.* 109 <https://doi.org/10.1029/2003JA010193>.
- Franco, A.M.S., Franz, M., Echer, E., Bolzan, M.J.A., 2020. Wavelet analysis of low frequency plasma oscillations in the magnetosheath of mars. *Adv. Space Res.* 65, 2090–2098. <https://doi.org/10.1016/j.asr.2019.09.009>.
- Gedalin, M., Newbury, J.A., Russell, C.T., 1998. Shock profile analysis using wavelet transform. *J. Geophys. Res.* 103, 6503–6511 ([doi:https://doi.org/10.1029/1997JA01998](https://doi.org/10.1029/1997JA01998)).
- Jackman, C.M., Thomsen, M.F., Dougherty, M.K., 2019. Survey of saturn's magnetopause and bow shock positions over the entire cassini mission: boundary statistical properties and exploration of associated upstream conditions. *J. Geophys. Res. Space Phys.* 124, 85–89. <https://doi.org/10.1029/2019JA026628>.
- Jelínek, K., Némecék, Z., Safránková, J., 2012. A new approach to magnetopause and bow shock modeling based on automated region identification. *J. Geophys. Res.* 117, A05208. <https://doi.org/10.1029/2011JA017252>.
- Kivelson, M., Bagenal, F., 2007. Chapter 7. planetary magnetospheres. *AAS/Div. Extrem. Solar Syst. Abstr.* 519–540. <https://doi.org/10.1016/B978-012088589-3/50032-3>.
- Kivelson, M.G., 2007. Planetary magnetospheres. *Handbook of Space Environment* 103, 469–492. [https://doi.org/10.1007/978-3-540-46315-3\\_19](https://doi.org/10.1007/978-3-540-46315-3_19).
- Kumar, Foufoula-Georgiou, 1997. Wavelet analysis for geophysical applications. *Rev. Geophys.* 35, 385–412 ([doi:https://doi.org/10.1029/1997RG000129](https://doi.org/10.1029/1997RG000129)).
- Martinecz, C., Fränz, M., Woch, J., Krupp, N., Roussos, E., Dubinin, E., Motschmann, U., Barabash, S., Lundin, R., Holmström, M., Andersson, H., Yamauchi, M., Grigoriev, A., Futaana, Y., Brinkfeldt, K., Gunell, H., Frahm, R.A., Wingham, J.D., Sharber, J.R., Scherer, J., Coates, A.J., Linder, D.R., Kataria, D.O., Kallio, E., Sales, T., Schmidt, W., Riihela, P., Koskinen, H.E.J., Kozyra, J.U., Luhmann, J., Russell, C.T., Roelof, E.C., Brandt, P., Curtis, C.C., Hsieh, K.C., Sandel, B.R., Grande, M., Sauvad, J.A., Fedorov, A., Thocaven, J.J., Mazelle, C., McKenna-Lawler, S., Orsini, S., Cerulli-Irelli, R., Maggi, M., Mura, A., Millilo, A., Wurz, P., Galli, A., Bochsler, P., Asamura, K., Szego, K., Baumjohann, W., Zhang, T.L., Lammer, H., 2008. Location of the bow shock and ion composition boundaries at venus—initial determinations from venus express aspera-4. *Planet. Space Sci.* 486, 780–784.
- Percival, D.B., Walden, A.T., 2000. *Wavelet Methods for Time Series Analysis*. Cambridge University Press.
- Russell, C.T., 2001. The dynamics of planetary magnetospheres. *Planet. Space Sci.* 49, 1005–1030. [https://doi.org/10.1016/S0032-0633\(01\)00017-4](https://doi.org/10.1016/S0032-0633(01)00017-4).
- Slavin, J., 2004. Mercury's magnetosphere. *Adv. Space Res.* 33, 1859–1874. <https://doi.org/10.1016/j.asr.2003.02.019>.
- Slavin, J., Baker, D., Gershman, D., Ho, G., Imber, S., Krimigis, S., 2020. *Mercury's Dynamic Magnetosphere*, pp. 461–496.
- Slavin, J.A., Acuna, M.H., Anderson, B.J., Baker, D.N., Benna, M., Gloeckler, G., Gold, R. E., Ho, G.C., Killen, R.M., Korth, H., Krimigis, S.M., McNutt Jr., R.L., Nittler, L.R., Raines, J.M., Schriver, D., Solomon, S.C., Starr, R.D., Trávníček, P., Zurbuchen, T.H., 2008. Mercury's magnetosphere after messenger's first flyby. *Science* 321, 85–89. <https://doi.org/10.1126/science.1159040>.
- Southwood, D.J., Chané, E., 2016. High-latitude circulation in giant planet magnetospheres. URL: *J. Geophys. Res.: Space Phys.* 121, 5394–5403. <https://doi.org/10.1002/2015JA022310>. arXiv:<https://agupubs.onlinelibrary.wiley.com/doi/pdf/10.1002/2015JA022310>. <https://agupubs.onlinelibrary.wiley.com/doi/abs/10.1002/2015JA022310>.
- Stern, D.P., Ness, N.F., 1982. Planetary magnetospheres. *Annu. Rev. Astron. Astrophys.* 20, 139–161. <https://doi.org/10.1146/annurev.aa.20.090182.001035>.
- Tarasov, V., Dubinin, E., Perraut, S., Roux, A., Sauer, K., Skalsky, A., Delva, M., 1998. Wavelet application to the magnetic field turbulence in the upstream region of the martian bow shock. *Earth Planets Space* 50, 699–708. <https://doi.org/10.1186/BF03352163>.
- Torrence, C., Compo, G.P., 1998. A practical guide to wavelet analysis. *Bull. Am. Meteorol. Soc.* 79, 61–78. [https://doi.org/10.1175/1520-0477\(1998\)079<0061:APGTA>2.0.CO;2](https://doi.org/10.1175/1520-0477(1998)079<0061:APGTA>2.0.CO;2).
- Waite, J.H., Combi, M.R., Ip, W.H., Cravens, T.E., McNutt, R.L., Kasprzak, W., Yelle, R., Luhmann, J., Niemann, H., Gell, D., Magee, B., Fletcher, G., Lunine, J., Tseng, W.L., 2006. Cassini ion and neutral mass spectrometer: Enceladus plume composition and structure. URL: *Science* 311, 1419–1422. <https://doi.org/10.1126/science.1121290>. arXiv:<https://science.sciencemag.org/content/311/5766/1419.full.pdf>. <https://science.sciencemag.org/content/311/5766/1419>.